

CONTENTS

1. Introduction	2
Main contributions	3
Outline	5
2. Analytical model	5
2.1. Analogy with the Stefan problem	5
2.2. Governing equation	6
2.3. Solution for a vertical planar damage front	8
2.4. Approximate Expression for the damage front position	9
2.5. Effect of gravity on the damage front position	12
2.6. Damage for spherical geometry	14
2.7. Thermally induced damage	15
3. Surface flow rate for constant pressure injection	16
3.1. Flow rate for the case of no damage	16
3.2. Flow rate for the case of a spherical damage front	17
4. Discussion	18
4.1. The limit $\Delta\phi \rightarrow 0$	18
4.2. Variation in density due to movement of the front	19
4.3. Field data comparison	19
5. Conclusion	22
Acknowledgements	23
Appendix A. Justification for neglecting $\nabla\rho$	23
References	24

A MODEL FOR TRACKING FRONTS OF STRESS-INDUCED PERMEABILITY ENHANCEMENT

K.C. LEWIS, SATISH KARRA AND SHARAD KELKAR

ABSTRACT. Using an analogy to the classical Stefan problem, we construct evolution equations for the fluid pore pressure on both sides of a propagating stress-induced damage front. Closed form expressions are derived for the position of the damage front as a function of time for the cases of thermally-induced damage as well as damage induced by over-pressure. We derive expressions for the flow rate during constant pressure fluid injection from the surface corresponding to a spherically shaped subsurface damage front. Finally, our model results suggest an interpretation of field data obtained during constant pressure fluid injection over the course of 16 days at an injection site near Desert Peak, NV.

1. INTRODUCTION

The formation and propagation of subsurface stress-induced damage zones is of great practical interest for oil extraction, geothermal energy, and CO₂ sequestration (e.g., [15], [18], [9], [5]). For all three applications, it is desirable to understand how human activities may affect permeability in the subsurface. In order to achieve this goal, it is important to understand a complex array of interrelated factors including local geological features, the in situ stress state, and which of several modes of stress-induced failure are most likely to dominate in a given scenario.

Two commonly employed mechanical failure criteria are the tensile and Mohr-Coulomb criteria. The type of rock failure likely to occur is governed by the conditions of in situ stress and the pressure of the fluid being injected. If the injection pressure is high enough to exceed the minimum principle in situ stress, a tensile “hydraulic fracture” is created. Walls

Corresponding Author: K.C. Lewis, Computational Earth Sciences Group, Earth and Environmental Sciences Division, Los Alamos National Laboratory (LANL), Los Alamos, NM 87545, United States of America. Phone: 505-665-6803 Email: kaylal@lanl.gov.

13 of the fracture are pushed open by the fluid pressure creating a high permeability pathway
14 through which the injected fluid can flow along the hydraulic fracture. The permeability of
15 such an open fracture is commonly represented by a cubic law, where the permeability at
16 any point in the fracture varies as the cube of the local fracture aperture and an empirically
17 determined friction factor. Published results ([10]) show that the aperture, and hence the
18 permeability, of such a hydraulic fracture varies smoothly over the majority of the fracture
19 length, dropping sharply to a very small value near the crack tip. For examples of analytic
20 studies of tensile fracture propagation, see [6], [7], and [17].

21 Rock failure can also occur at fluid pressures below the minimum principle earth stress
22 through the mechanism of shearing. Such failure is often described using the Mohr-Coulomb
23 criterion (for more detail, see [8]). The determining quantity in this case is the relative
24 magnitude of the shear stress and the effective normal stress in the rock. The effective
25 normal stress decreases as the fluid pressure increases. When the rock fails in shear, the
26 fractures can dilate but do not display large aperture widening as in the case of hydraulic
27 fractures, although a significant increase in permeability does take place in the plane of
28 failure ([12], [13]). The situation is more complex than that of a fracture open in tension,
29 and there are no simple analytical expressions relating fracture geometry to permeability
30 that are widely applicable. Published results ([10]) show an increase in permeability by
31 factors up to 100 or so under shear failure.

32 **Main contributions.** A complete analysis of the problem requires solving the coupled
33 nonlinear equations of fluid flow, heat transfer, and mechanical deformation of the rock mass,
34 necessitating the use of numerical models. However, useful insight into the behavior of the
35 system can be obtained using simplified conceptual models that allow the system of governing
36 equations to be decoupled. We solve the fluid flow problem, while incorporating the influence
37 of the mechanical deformation and rock failure aspects implicitly through a prescribed step
38 change in the permeability, with a low permeability for rock in an undamaged state and
39 a higher permeability for rock that is in a fully damaged state. That is, we conceptualize

40 the system as comprised of two zones - a zone containing the rock at pre-failure conditions
 41 and a second zone with post-failure conditions in the rock. Simplification is introduced by
 42 treating rock permeability and porosity as constant within each zone, with an abrupt change
 43 in the transition zone, which we approximate as infinitely thin. Further, we take the ratio
 44 of the post-failure to pre-failure permeability to be an empirically determined constant. We
 45 study two modes of failure. In the first, rock failure is driven by high fluid pressure, with a
 46 fixed specified pressure above which rock failure occurs and below which no damage occurs.
 47 We take this threshold pressure to be constant, which assumes an isothermal environment
 48 as well as an approximately uniform initial stress field. In the second case, rock failure is
 49 driven thermally due to a large temperature difference between fluid and the surrounding
 50 medium (see, e.g., [1] and [16]). While in this case there is no assumed threshold pressure,
 51 our analysis does assume that differences in stress between one side of a propagating damage
 52 front and the other are approximately constant in time as the front propagates.

53 Using these assumptions we derive approximate expressions for the position of the interface
 54 between damaged and undamaged regions during failure of a porous matrix induced by fluid
 55 injection. Afterward, we show how to relate these expressions to the mass flow rate during
 56 constant pressure injection, which is a commonly employed observable quantity. Finally, we
 57 show how our model leads to one plausible interpretation of flow rate data obtained during
 58 constant pressure injection at a site near Desert Peak, Nevada. The following are the main
 59 contributions of this paper:

- 60 (1) The model we present can be used to predict the position of the damage front without
 61 explicitly solving the coupled equations governing stress and fluid flow.
- 62 (2) The model relates subsurface damage to mass flow rates during constant pressure
 63 fluid injection.
- 64 (3) The model includes no assumption regarding whether failure occurs as a result of
 65 tension or shear.
- 66 (4) The model is a new application of the Stefan-type solution method.

Outline. In section 2.1 we first draw an analogy with the Stefan problem and present the governing equations. Then we present an analytical expression for the position of, and pore pressures on either side of, a vertical damage front; we then derive an approximate closed form expression for the position of the front in section 2.4. Next, in section 2.5, we show that the effect of gravity is small for sufficiently small times. We then adapt our model to calculate the approximate damage front position in the case of thermally driven failure. Expressions for flow rates under constant pressure injection for spherical damage front geometry are derived in section 3 followed by comparison of the closed form solutions from our model with the field data from Desert Peak, Nevada in section 4.

2. ANALYTICAL MODEL

2.1. Analogy with the Stefan problem. Consider a semi-infinite horizontal slab of fully saturated porous material with a high pore pressure, p_H , maintained at the left end and such that, at all times, the pressure approaches a much lower pressure p_L as x approaches infinity. The initial pressure is p_L everywhere, and material properties are initially uniform. Following the discussion of last section, we assume that there is a sharp boundary separating damaged and undamaged material. At times $t > 0$ a damage front will travel in the positive x direction, and all positions to the left of the front will be in the “damage” zone. On the other hand, all points to right of this point will have their initial permeabilities and porosities. The permeability is clearly a function of pressure, being a higher value on the left side of the damage front than on the right side; this pressure dependence causes the mass balance equation (see below) to become nonlinear. However, the constancy of material properties on either side of the damage front motivates the idea of splitting the solution domain into two halves, solving linear mass balance equations on each half, and pasting the resulting solutions together at the damage front. This situation is exactly analogous to that in the classical Stefan problem (see [3], [14]).

In one version of the classical Stefan problem, the half plane corresponding to $x \leq 0$ is filled with ice while that corresponding to $x > 0$ is filled with liquid water. As time progresses, an

ice front propagates toward positive values of x as the ice phase removes heat from the liquid. The problem is to solve for both the temperature as a function of time and space for all $x > 0$ and the position of the ice-water interface as a function of time. Mathematical problems of a similar type arise in the study of systems that have moving boundaries separating regions with distinct physical properties (for many such examples, see [14]).

2.2. Governing equation. On each side of the damage front the permeability and porosity are taken as constants, but such that each displays a discrete jump in crossing from one side of the front to the other. The fluid on each side of the damage front therefore obeys a mass conservation equation

$$\frac{\partial(\rho\phi_i)}{\partial t} + \nabla \cdot (\rho\mathbf{v}_i) = 0, \quad (2.1)$$

where ρ is the fluid density, ϕ is the porosity, \mathbf{v} is the volumetric flux, and the subscript $i = 1, 2$, represents the damaged or undamaged side of the front. The volumetric flux is given by Darcy's law

$$\mathbf{v}_i = -\frac{k_i}{\mu} (\nabla p_i + \rho g \nabla z), \quad (2.2)$$

where k is the permeability, μ is the dynamic viscosity, p is the pressure, g is the gravitational acceleration, and z is the vertical coordinate taken as positive upward. We include variations in the fluid density only in the unsteady term and neglect the gradient of the fluid density (see the Appendix for a detailed justification of this assumption). On each side of the front, the porosity and the density are related to the pressure via

$$\phi_i = \phi_{i0} + \alpha(p_i - p_0), \quad (2.3)$$

and

$$\rho = \rho_0[1 + \beta(p_i - p_0)], \quad (2.4)$$

where α is a constant, β is the fluid compressibility, and the subscript zero refers to initial values. The reasoning leading to (2.3) can be found in [11]. The increase in ϕ in crossing from the undamaged to the damaged side of the front is assumed constant and equal to

119 $\Delta\phi \equiv \phi_1 - \phi_2$. Combining (2.1) through (2.4), we obtain

$$120 \quad \frac{\partial p_i}{\partial t} - a_i \nabla^2 p_i = 0, \quad (2.5)$$

121 where

$$122 \quad a_i \equiv \frac{k_i}{\mu(\phi_i\beta + \alpha)} \equiv \frac{k_i}{\mu\gamma_i}, \quad (2.6)$$

123 and where γ_i is the total compressibility (liquid plus porous medium) in region i . We impose
124 the boundary conditions

$$p_1(\mathbf{r} = \mathbf{0}, t) = p_H,$$

$$125 \quad p_2(\mathbf{r} \rightarrow \infty, t) = p_L, \quad (2.7)$$

$$p_1(\mathbf{r} = \mathbf{R}, t) = p_2(\mathbf{r} = \mathbf{R}, t) = p_D,$$

126 where $\mathbf{R}(t)$ is the position of the damage zone at time t , $p_2(\mathbf{r} \rightarrow \infty, t)$ is an abbreviation for
127 the value of p_2 as $|\mathbf{r}|$ approaches infinity, and p_D is defined as the pore pressure at the damage
128 front. For uniqueness of the solution, one more boundary condition must be imposed at the
129 damage front. Over an increment of time, the fluid mass into the interior (damaged) side of
130 the damage front must equal that out of the exterior (undamaged) side minus the amount
131 of fluid taken up by an increase in pore volume due to progression of the front. Requiring
132 mass conservation across an element of area A of damage front over a time Δt thus yields
133 the boundary condition

$$134 \quad A\Delta t\rho\mathbf{v}\Big|_{\mathbf{r}=\mathbf{R}^-} \cdot \hat{\mathbf{n}} = A\Delta t\rho\mathbf{v}\Big|_{\mathbf{r}=\mathbf{R}^+} \cdot \hat{\mathbf{n}} + \rho\Delta\phi\Delta V, \quad (2.8)$$

135 where ΔV is the total volume traversed by the front over Δt , $\Delta\phi \equiv \phi_1 - \phi_2 > 0$, and $\hat{\mathbf{n}}$ is
136 the unit normal to A (see figure 1). In (2.8) we have neglected variations in fluid density
137 due to progression of the damage front; this we justify in section (4.2). Substituting (2.2)

138 into (2.8) gives the final boundary condition as

$$139 \quad k_1 (\nabla p_1 + \rho g \nabla z) \cdot \hat{\mathbf{n}} = k_2 (\nabla p_2 + \rho g \nabla z) \cdot \hat{\mathbf{n}} - \mu \Delta \phi \frac{1}{A} \frac{dV}{dt}. \quad (2.9)$$

140 **2.3. Solution for a vertical planar damage front.** If the damage front is assumed to be
 141 a vertical plane, and if the fluid flux parallel to the plane of the front is negligible compared
 142 to the flux normal to the plane of damage, then (2.5) becomes

$$143 \quad \frac{\partial p_i}{\partial t} - a_i \frac{\partial^2 p_i}{\partial x^2} = 0, \quad (2.10)$$

144 and equation (2.9) becomes

$$145 \quad k_1 \left. \frac{\partial p_1}{\partial x} \right|_{x=X} = k_2 \left. \frac{\partial p_2}{\partial x} \right|_{x=X} - \mu \Delta \phi \frac{dX}{dt}, \quad (2.11)$$

146 where the damage front is located at $x = X$. The partial differential equation plus boundary
 147 and initial conditions given above can be solved exactly as in [3], pg. 285, with the substi-
 148 tutions $p \mapsto v, p_H \mapsto 0, p_D \mapsto T_1, p_L \mapsto V, a \mapsto \kappa, k \mapsto K$, and $\mu \Delta \phi \mapsto L\rho$; however, for the
 149 convenience of the reader we now briefly recapitulate the argument leading to a solution.

150 Scale analysis suggests that the solution to (2.10) depends only on the dimensionless
 151 combination $x/\sqrt{a_i t}$ (see [2]). Substituting p as a function of $x/\sqrt{a_i t}$ into (2.10) results in
 152 an ordinary differential equation that can be easily integrated to give the solution

$$153 \quad p_i(x, t) = \frac{2C_i}{\sqrt{\pi}} \int_0^{x/\sqrt{t}} e^{-\zeta^2/4a_i} d\zeta + D_i = C_i \operatorname{erf} \left(\frac{x}{2\sqrt{a_i t}} \right) + D_i, \quad (2.12)$$

154 where erf is the error function, defined as

$$155 \quad \operatorname{erf}(x) \equiv \frac{2}{\sqrt{\pi}} \int_0^x e^{-z^2} dz. \quad (2.13)$$

156 The first two boundary conditions from (2.7) yield

$$D_1 = p_H, \quad (2.14)$$

$$D_2 = p_L - C_2,$$

158 so that it only remains to find the constants C_1 and C_2 . The third of equations (2.7) yields

$$C_1 \operatorname{erf} \left(\frac{X}{2\sqrt{a_1 t}} \right) + p_H = C_2 \left[\operatorname{erf} \left(\frac{X}{2\sqrt{a_2 t}} \right) - 1 \right] + p_L = p_D. \quad (2.15)$$

160 The first and middle expressions can only be equal to the constant on the right if $X = \lambda\sqrt{t}$
 161 for some constant λ . Substituting this expression for X into (2.15) allows one to solve for
 162 both C_1 and C_2 as functions of the undetermined constant λ . Application of condition (2.11)
 163 then results in the equation

$$\frac{k_1 C_1(\lambda) e^{\frac{-\lambda^2}{4a_1}}}{\sqrt{a_1}} = \frac{k_2 C_2(\lambda) e^{\frac{-\lambda^2}{4a_2}}}{\sqrt{a_2}} - \frac{\mu \Delta \phi \lambda \sqrt{\pi}}{2}, \quad (2.16)$$

165 which determines λ implicitly. In general, equation (2.16) can be solved for λ only numeri-
 166 cally in combination with the constraints on C_1 and C_2 from equations (2.15); however, in
 167 the next section we show how to obtain an approximate closed form expression for $X = \lambda\sqrt{t}$.

168 **2.4. Approximate Expression for the damage front position.** In the absence of any
 169 damage, i.e., $a_1 = a_2 \equiv a$, the effect of the high pressure at $x = 0$ is governed by (2.10) and
 170 will travel a distance L in time t given approximately by the characteristic diffusive length
 171 scale

$$L = \sqrt{at}. \quad (2.17)$$

173 In fact, the form of this length scale does not depend on the problem geometry - it depends
 174 only on the fact that the relevant process is one of diffusion ([2], [3]). In the case of a
 175 propagating damage front, the pressure at the $x = 0$ boundary has influenced that at the
 176 damage front, by definition, enough to raise the pressure there to p_D . Furthermore, the
 177 speed at which an effect from the high pressure boundary can propagate is limited by the

178 lower permeability of the undamaged region as well as by increased fluid storage due to the
 179 porosity increase upon damage. Therefore, the diffusive time scale for region one is short
 180 compared to that governing the movement of the damage front; this fact implies that the
 181 pressure in region one at all times assumes approximately a linear steady-state profile with
 182 gradient

$$183 \quad \frac{\partial p_1}{\partial x} \approx \frac{p_D - p_H}{X} \equiv -\frac{\Delta p_1}{X}. \quad (2.18)$$

184 This approximation improves as p_D approaches p_H . In region two, the pressure effect from the
 185 damage front propagates to roughly the distance $\sqrt{a_2 t}$ in time t . Therefore, an approximation
 186 similar to (2.18), using the distance $\sqrt{a_2 t}$ instead of X , can be used to estimate $\partial p_2 / \partial x$; the
 187 approximate pressure gradient in region two is given as

$$188 \quad \frac{\partial p_2}{\partial x} \approx \frac{p_L - p_D}{\sqrt{a_2 t}} \equiv -\frac{\Delta p_2}{\sqrt{a_2 t}}. \quad (2.19)$$

189 See Figure 2 for a comparison between (2.18) and (2.19) and the exact solution slopes given
 190 by (2.12). Putting (2.18) and (2.19) into (2.11) leads to

$$191 \quad \frac{k_1 \Delta p_1}{X} = \frac{k_2 \Delta p_2}{\sqrt{a_2 t}} + \mu \Delta \phi \frac{dX}{dt}. \quad (2.20)$$

192 We search for a solution of the form $X = \lambda t^n$ for some undetermined n . Putting this
 193 expression into (2.20) yields

$$\frac{k_1 \Delta p_1}{\lambda} t^{-n} - \frac{k_2 \Delta p_2}{\sqrt{a_2}} t^{-1/2} - \mu \Delta \phi \lambda n t^{n-1} = 0. \quad (2.21)$$

194 The only way that this equation can be satisfied for all times is for the powers of t to equal
 195 one another; the only value of n for which such is the case is $n = 1/2$. X therefore takes the
 196 form $\lambda \sqrt{t}$ and (2.20) becomes

$$197 \quad \lambda^2 + \left(\frac{2k_2 \Delta p_2}{\mu \Delta \phi \sqrt{a_2}} \right) \lambda - \frac{2k_1 \Delta p_1}{\mu \Delta \phi} = 0. \quad (2.22)$$

198 There is only one positive root of this equation, leading to the approximate damage front
 199 position

$$200 \quad X = \left(-\frac{k_2 \Delta p_2}{\mu \Delta \phi \sqrt{a_2}} + \sqrt{\frac{k_2^2 \Delta p_2^2}{\mu^2 \Delta \phi^2 a_2} + \frac{2k_1 \Delta p_1}{\mu \Delta \phi}} \right) \sqrt{t}. \quad (2.23)$$

201 Table 1 shows values of λ calculated from (2.23) and values computed numerically from
 202 equation (2.16) via the bisection method for a wide range of permeabilities and porosities
 203 for the damaged and undamaged zones. Every row in the table corresponds to $p_H = 3$
 204 MPa, $p_L = 0.1$ MPa, $p_D = 1.5$ MPa, $\mu = 10^{-3}$ Pa \cdot s, and $\gamma = 10^{-10}$ Pa $^{-1}$, but the results
 205 are not very sensitive to changes in these parameters. We note that the relative error with
 206 respect to the computationally derived value of λ does not exceed three percent. The largest
 207 relative errors occur when flow on the exterior side of the damage front is largest, because
 208 approximation (2.19) is not as good an approximation as (2.18).

209 The expression for λ can be further simplified if there is a large contrast in the porosity
 210 and permeability on crossing from one side of the damage front to the other. To affect the
 211 simplification, we first re-write the approximate expression for λ as

$$212 \quad \lambda \approx -\frac{k_2 \Delta p_2}{\mu \Delta \phi \sqrt{a_2}} + \sqrt{\frac{2k_1 \Delta p_1}{\mu \Delta \phi}} \sqrt{\frac{k_2^2 \Delta p_2^2}{2k_1 \Delta p_1 \mu \Delta \phi a_2} + 1}. \quad (2.24)$$

213 The second term on the right side is greater than

$$214 \quad \sqrt{\frac{2k_1 \Delta p_1}{\mu \Delta \phi}}, \quad (2.25)$$

215 so if the absolute value of the first term on the right side of (2.24) is much less than this
 216 quantity, it may be neglected. This condition may be written as

$$217 \quad \frac{k_2^2 \Delta p_2^2}{\mu^2 \Delta \phi^2 a_2} \ll \frac{2k_1 \Delta p_1}{\mu \Delta \phi}, \quad (2.26)$$

218 which is completely equivalent to

$$219 \quad \frac{k_2^2 \Delta p_2^2}{2k_1 \Delta p_1 \mu \Delta \phi a_2} \ll 1. \quad (2.27)$$

Therefore, if (2.27) holds, the first term on the right side of (2.24) may be neglected. But (2.27) is also the condition that the factor multiplying (2.25) in equation (2.24) is approximately equal to unity. Satisfaction of condition (2.27) therefore results in

$$\lambda \approx \sqrt{\frac{2k_1\Delta p_1}{\mu\Delta\phi}}. \quad (2.28)$$

Condition (2.27) can be made more transparent by using (2.6) to eliminate a_2 and assuming that $\Delta p_2 \approx \Delta p_1$. Then (2.27) takes the form

$$\frac{\gamma_2 k_2 \Delta p_1}{2k_1 \Delta\phi} \ll 1. \quad (2.29)$$

Hence, if the contrast in material properties between regions one and two is large enough to satisfy (2.29), equation (2.28) may be employed to estimate the position of the damage front as $X \approx \lambda\sqrt{t}$. Equation (2.28) is the same expression that would have been obtained if flow across the damage front had been neglected in equation (2.20), i.e., if the term involving $\partial p_2 / \partial x$ had been neglected. Therefore, condition (2.29) is also the condition that flow across the damage front toward the lower permeability region may be neglected in determining the position of the front. As an example, if $\gamma_2 = 10^{-10} \text{ Pa}^{-1}$, $k_2 = 10^{-16} \text{ m}^2$, $\Delta p_1 = 10^6 \text{ Pa}$, $k_1 = 10^{-14} \text{ m}^2$, and $\Delta\phi = 0.1$, the quantity on the left hand side of (2.29) is equal to 0.5×10^{-5} .

2.5. Effect of gravity on the damage front position. In the previous section we assumed that the damage front is a vertical planar surface; gravity did not appear in the boundary or initial conditions because fluid flow in the vertical direction was assumed negligible compared to that in the horizontal direction. We now consider the case such that the damage front is a horizontal planar surface and vertical fluid flow dominates. The presence of gravity in the volumetric flux gives rise to a boundary condition that prevents the method of solution employed section 2.3; however, it is still possible to derive an approximate formula for the position of the damage front.

In the present case, equation (2.9) becomes

$$k_1 \left(\frac{\partial p_1}{\partial z} + \rho g \right) = k_2 \left(\frac{\partial p_2}{\partial z} + \rho g \right) - \mu \Delta \phi \frac{dZ}{dt}. \quad (2.30)$$

If condition (2.29) holds, we may neglect flow across the damage front. Then, by using (2.18), equation (2.30) may be written in the form

$$\frac{\Delta p_1}{\Delta p_2} \approx \Delta \phi \left(\frac{\mu Z}{k_1 \Delta p_2} \frac{dZ}{dt} \right) + \frac{\rho g Z}{\Delta p_2}. \quad (2.31)$$

This equation cannot be easily integrated, but a useful solution can still be obtained by noting that the second term on the right hand side is small relative to unity when

$$\frac{\rho g}{\Delta p_2} \ll \frac{1}{Z}. \quad (2.32)$$

For typical orders of magnitude of the quantities on the left hand side, this inequality becomes $Z \ll 100$ m. When this condition holds, we may take $\epsilon \equiv \rho g / \Delta p_2$ as a small parameter. The solution may then be represented as a perturbative series

$$Z(t) = \sum_{n=0}^{\infty} Z_n(t) \epsilon^n. \quad (2.33)$$

Substituting (2.33) into (2.31), setting coefficients of differing powers of ϵ equal to zero, and neglecting powers of ϵ greater than unity yields the equations

$$\frac{\Delta \phi \mu}{k_1 \Delta p_1} Z_0 \frac{dZ_0}{dt} = 1, \quad (2.34)$$

and

$$\frac{dZ_1}{dt} + \frac{Z_1}{2t} = -\frac{k_1 \Delta p_1}{\Delta \phi \mu}. \quad (2.35)$$

This equation is dimensionally homogeneous because Z_1 has dimensions of length squared, due to ϵ having dimensions of 1/length. The initial condition for these equations is $Z_{0,1}(0) =$

263 0. Equation (2.34) has the solution

$$264 \quad Z_0 = \sqrt{\frac{2k_1\Delta p_1}{\mu\Delta\phi}}t. \quad (2.36)$$

265 Equation (2.35) can be easily integrated to give

$$266 \quad Z_1 = -\frac{2k_1\rho gt}{3\Delta\phi\mu}, \quad (2.37)$$

267 so that the perturbed solution to first order is

$$268 \quad Z(t) \approx \sqrt{\frac{2k_1\Delta p_1}{\mu\Delta\phi}}t - \frac{2k_1\rho gt}{3\Delta\phi\mu}. \quad (2.38)$$

269 The ratio of the second term on the right hand side to the first is

$$270 \quad \frac{\rho g}{3} \sqrt{\frac{2k_1 t}{\mu\Delta p_1}}, \quad (2.39)$$

271 and this term is small compared to unity for sufficiently small times. For example, if $k_1 =$
 272 10^{-13} m^2 , the correction is small for times that are small compared to ten days. The effect
 273 of gravity is to slow the progression of an upward moving front, and this effect is more
 274 pronounced as t , or equivalently Z , increases (“equivalently” because Z is monotonically
 275 increasing in t).

276 **2.6. Damage for spherical geometry.** In spherical coordinates, the steady-state solution
 277 to (2.5) does not have the simple linear profile employed above; therefore, we separately
 278 derive a formula for the approximate damage front position in spherical geometry. In the
 279 steady state and in spherical coordinates with radial symmetry, equation (2.5) becomes

$$280 \quad \frac{d^2(rp_i)}{dr^2} = 0. \quad (2.40)$$

281 The solution to this equation is readily found to be

$$282 \quad p_i(r) = C_1 + \frac{C_2}{r}, \quad (2.41)$$

where C_1 and C_2 are constants. The pressure profiles in the damaged and undamaged zones are then approximately (using reasoning similar to that in section 2.4)

$$p_1(r) = p_H - \frac{R\Delta p_1}{R - r_0} \left(1 - \frac{r_0}{r}\right), \quad (2.42)$$

and

$$p_2(r) = p_D - \frac{\Delta p_2 \sqrt{a_2 t}}{\sqrt{a_2 t} - R} \left(1 - \frac{R}{r}\right), \quad (2.43)$$

where r_0 is the radius of the injection well, i.e., $p_1(r_0) = p_H$. Using these expressions, condition (2.9) becomes

$$\frac{k_1 \Delta p_1 r_0}{R(R - r_0)} = \frac{k_2 \Delta p_2 \sqrt{a_2 t}}{R(\sqrt{a_2 t} - R)} + \mu \Delta \phi \frac{dR}{dt}. \quad (2.44)$$

To affect a solution, we consider the case where $k_2/k_1 \ll 1$ and $r_0/R \ll 1$. Then (2.44) becomes

$$\frac{k_1 \Delta p_1 r_0}{\mu \Delta \phi} = R^2 \frac{dR}{dt}, \quad (2.45)$$

which is separable and has the solution

$$R = \left(r_0^3 + \frac{3k_1 \Delta p_1 r_0 t}{\mu \Delta \phi} \right)^{\frac{1}{3}}. \quad (2.46)$$

2.7. Thermally induced damage. When damage is driven by thermal effects rather than over-pressure, it is no longer reasonable to assume that the pressure at the damage front is approximately constant. We will now explore the consequences of letting p_D vary, from $p_D = p_H$ when the front is at the injection source to $p_D = p_L$ as the front approaches infinity. The simplest assumption consistent with this behavior is that $p_H - p_D$ increases linearly with $R - r_0$. That is,

$$\Delta p_1 = \frac{\Delta p (R - r_0)}{R_{max} - r_0} \equiv D(R - r_0), \quad (2.47)$$

where R_{max} is the distance at which $\Delta p_1 = p_H - p_\infty \equiv \Delta p$. In the following, we will only consider the system behavior for $r_0 < R_{max}$. In the case of spherical geometry, we substitute

305 (2.47) into (2.44) and again assume that $k_2/k_1 \ll 1$, obtaining

$$306 \quad \frac{k_1 D r_0}{\mu \Delta \phi} = R \frac{dR}{dt}, \quad (2.48)$$

307 which has the solution

$$308 \quad R = \sqrt{r_0^2 + \frac{2k_1 \Delta p r_0 t}{\mu \Delta \phi (R_{max} - r_0)}}. \quad (2.49)$$

309 If t_{max} is the time at which $R = R_{max}$, we may solve for R_{max} in terms of this time as

$$310 \quad R_{max} = \left(\frac{2k_1 \Delta p r_0 t_{max}}{\mu \Delta \phi} \right)^{\frac{1}{3}}, \quad (2.50)$$

311 where we have assumed that $r_0/R_{max} \ll 1$. Figure 3 shows a comparison between front
 312 positions predicted via (2.49) versus (2.46), using the parameters shown in Table 2 and
 313 $\Delta \phi = 10^{-2}$.

314 According to this model, then, the damage front progresses much faster in the case of
 315 thermally driven damage than in the case of pressure driven damage. This behavior results
 316 from the fact that, when Δp_1 increases with time, the mass flow on the damage-side of the
 317 damage front increases with time, and this increased flow drives the front forward much more
 318 quickly than when Δp_1 is constant, as in the pressure driven case.

319 3. SURFACE FLOW RATE FOR CONSTANT PRESSURE INJECTION

320 The fluid mass flow rate measured at the ground surface as a function of time is a commonly
 321 measured quantity in applications. We first derive an expression for the flow rate in the
 322 absence of damage. Afterward, we show how to obtain predicted flow rate for a spherical
 323 subsurface failure front geometry.

324 **3.1. Flow rate for the case of no damage.** Consider the case of fluid injection at con-
 325 stant pressure p_H into a homogeneous medium of pressure $p_L < p_H$, and with no ensuing
 326 damage front. In this case, a pressure pulse spreads out radially from the injection point to
 327 approximately the radius \sqrt{at} after a passage of time t . Using (2.41), we approximate the

328 pressure profile as

$$329 \quad p(r) \approx p_H - \frac{\Delta p \sqrt{at}}{\sqrt{at} - r_0} \left(1 - \frac{r_0}{r}\right). \quad (3.1)$$

330 The pressure gradient near the injection point is thus

$$331 \quad \frac{dp}{dr} \approx -\frac{\Delta p \sqrt{at}}{r_0(\sqrt{at} - r_0)}. \quad (3.2)$$

332 Neglecting gravitational effects and integrating the volumetric fluid flux over the surface of
333 a sphere of fixed radius r_0 yields the flow rate

$$334 \quad \mathcal{F}_0 \approx \frac{4\pi \rho k r_0 \Delta p \sqrt{at}}{\mu(\sqrt{at} - r_0)}. \quad (3.3)$$

335 Therefore, the flow rate is expected to approach the constant

$$336 \quad \frac{4\pi \rho k r_0 \Delta p}{\mu}, \quad (3.4)$$

337 as $t \rightarrow \infty$. This formula also describes the flow rate for the case of “full damage”, i.e., the
338 situation that prevails after a damage front has progressed as far as possible and damage
339 has ceased.

340 **3.2. Flow rate for the case of a spherical damage front.** We now consider the case
341 of an over-pressure induced spherically shaped propagating damage front. Using equation
342 (2.42) to calculate the volumetric flux at the injection well and integrating this flux over the
343 surface of a sphere with radius r_0 yields

$$344 \quad \mathcal{F}_{sph} = \frac{4\pi \rho k_1 \Delta p_1 r_0 R}{\mu(R - r_0)}, \quad (3.5)$$

345 where R is given by equation (2.46). This flow rate approaches (3.4) as $R \rightarrow \infty$, regar

$$\frac{d}{dt} \sqrt{\kappa t} = \frac{1}{2} \sqrt{\frac{\kappa}{t}} \quad (3.6)$$

where κ is the thermal diffusivity, regardless of the particular form that R takes. In the case of thermally induced damage, substituting (2.47) into (3.5) yields

$$\mathcal{F}_{sph} = \frac{4\pi\rho k_1 \Delta p r_0 R}{\mu(R_{max} - r_0)}, \quad (3.7)$$

where R is now given by (2.49). In this case we note that

$$\frac{\partial \mathcal{F}_{sph}}{\partial \Delta\phi} \approx \frac{4\pi\rho k_1 \Delta p r_0}{\mu} \left(\frac{1}{R_{max}} \frac{\partial R}{\partial \Delta\phi} - \frac{R}{R_{max}^2} \frac{\partial R_{max}}{\partial \Delta\phi} \right). \quad (3.8)$$

However, if $R \gg r_0$ and $R_{max} \gg r_0$ then

$$\frac{1}{R_{max}} \frac{\partial R}{\partial \Delta\phi} \approx -\frac{R}{3R_{max}\Delta\phi}, \quad (3.9)$$

and

$$\frac{R}{R_{max}^2} \frac{\partial R_{max}}{\partial \Delta\phi} = -\frac{R}{3R_{max}\Delta\phi}, \quad (3.10)$$

so that these terms in (3.8) exactly cancel one another. Hence, even though the position of the damage front depends on $\Delta\phi$, in the case of thermally driven damage the flow rate does not.

4. DISCUSSION

4.1. The limit $\Delta\phi \rightarrow 0$. Up until now we have assumed that, upon mechanical failure, the porosity increases. However, in some cases it is possible for the permeability to change by a large amount while the change in porosity is very small. It makes sense, then, to inquire into the possibility that the increase in porosity is zero or near zero; however, our formalism must be slightly altered in this case. For example, equation (2.24) can be written

$$\Delta\phi\lambda^2 + \frac{2k_2\Delta p_2}{\mu\sqrt{a_2}}\lambda - \frac{2k_1\Delta p_1}{\mu} = 0, \quad (4.1)$$

and in the limit $\Delta\phi \rightarrow 0$ the quadratic term vanishes. Hence, the correct formula in this case is not (2.24) but

$$\lambda \approx \frac{\sqrt{a_2}k_1\Delta p_1}{k_2\Delta p_2}. \quad (4.2)$$

368 In the case of zero damage, i.e., when $p_D = p_H$, the above equation gives $\lambda = 0$ as expected.

369 **4.2. Variation in density due to movement of the front.** We have neglected variations
 370 in fluid density resulting from movement of the damage front, but we now show that these
 371 variations are negligible. For the same case as in section 2.3, suppose that the damage front
 372 moves from position x_1 to x_2 over a small interval of time. Then the pressure at x_1 during
 373 this interval will have increased by amount

$$374 \quad \Delta p \approx -\left.\frac{\partial p_1}{\partial x}\right|_X \Delta X, \quad (4.3)$$

375 where $\Delta X \equiv x_2 - x_1$. This pressure increase, by (2.4), leads to an increase in density

$$376 \quad \Delta \rho \approx -\left.\frac{\partial p_1}{\partial x}\right|_X \Delta X \beta \rho_0. \quad (4.4)$$

377 Hence, the discrete form of condition (2.11), when modified to include this density variation,
 378 is

$$379 \quad -\left.\frac{k_1}{\mu} \frac{\partial p_1}{\partial x}\right|_{x=X} = -\left.\frac{k_2}{\mu} \frac{\partial p_2}{\partial x}\right|_{x=X} + \Delta \phi \frac{\Delta X}{\Delta t} \left(1 - \left.\frac{\partial p_1}{\partial x}\right|_X \beta \Delta X\right). \quad (4.5)$$

380 In the limit as $\Delta t \rightarrow 0$, equation (4.5) reduces to (2.11).

381 **4.3. Field data comparison.** Chabora et al. [4] have reported surface flow rate data
 382 during constant pressure subsurface injection over the course of 100 days for a site near
 383 Desert Peak, NV (see Figure 4, red circles). Most of the data was gathered within the first
 384 16 days, with one data point at 100 days. There is an interruption in data for about 3
 385 days starting at day 12 due to pump failure. Because the resumed flow rate curve strongly
 386 resembles a continuation of the initial curve at a later time, and because the time during
 387 cessation of pumping is small relative to the thermal relaxation time of the reservoir, we
 388 align the resumed curve with the initial one as shown also in Figure 4 (a “continuous” curve
 389 is depicted with red circles at earlier times and blue ones at later times). The resulting curve
 390 would likely have resulted if the pump had not failed. The temperature of the injected fluid
 391 was approximately 100°C at the subsurface injection point, while the in situ temperature was

approximately 190°C. On the other hand, the injection pressure was 13.1 MPa, compared to an in situ pressure of about 9 MPa; therefore, rock failure was likely dominated by effects of thermal contraction. Consequently, we employ formula (3.7) above to calculate flow rates associated with the rock failure. Because we are ignoring the effect of gravity, we attempt to match only the data from the first 16 days. The flow rate is approximately constant for the first several days, and according the formulae we have developed above, such a curve suggests that damage has no yet been initiated. We use a weight function to interpolate between the damage-free and spherical-damage-front solutions in the region where one regime begins to transition to the other. The weight function is taken as

$$w = 1 - \frac{1}{1 + \exp[-b(t - t_{shf} - \Delta t)]}, \quad (4.6)$$

where b is a constant with dimensions of inverse time, t_{shf} is the time at which the failure geometry begins to transition from lack of damage to a spherical damage mode, and Δt is the width of the region of overlap between these modes of failure. The total flow rate is thus

$$\mathcal{F} = w\mathcal{F}_0 + (1 - w)\mathcal{F}_{sph}. \quad (4.7)$$

Table 2 gives the values of the parameters used to fit the field data. Figure 5 shows the comparison between our model solution and the data. The blue curve is given by (4.7), the black curve is the predicted flow rate in the case of no damage, and the green curve shows the predicted flow rates for a spherical damage front only, all of these curves being calculated using the same model parameters. From equation (3.8), the choice of $\Delta\phi$ does not influence the flow rate.

When all observations are taken into account, the variables in our model are all constrained. The parameter Δt is determined by noting that the observed flow rates transition from constant to non-constant flow rates over a span of a few days. The transition time, t_{shf} , occurs at about five days after injection begins. If t_{shf} and Δt are expressed in units of days, b is then one inverse day, because it is a normalization factor converting time into

417 the dimensionless time that is appropriate for the argument of an exponential function. The
 418 injection and in situ far-field pressures are constrained from observation and from the hy-
 419 drostatic pressure profile, respectively. The fluid viscosity and density are determined from
 420 the average fluid pressure and temperature together with standard equations of state for
 421 pure water. The radius of the injection wellbore is known to be about $r_0 \approx 0.23$ m. For
 422 the pre-damage curve to match the flow rates at times less than five days, k_2 must be set
 423 equal to 10^{-14} m². For the flow rates corresponding to rock failure, R_{max} is determined from
 424 equation (2.50) and noting that the observed flow rate curve appears to level off starting at
 425 about forty days, giving $t_{max} \approx 40$ days (we are here assuming that the flattening of the
 426 curve starting at around this time corresponds to a transition to cessation of damage). We
 427 also note that, as $R_{max} \propto t_{max}^{1/3}$, the resulting flow rate is not very sensitive to the time chosen
 428 for t_{max} . The predicted curve corresponding to a spherical damage front (using (3.7)) can
 429 only match the observed flow rates past five days if k_2 is set to about 1.2×10^{-13} m² - about
 430 twelve times the pre-damage permeability.

431 If we assume that the damage front coincides at all times with some isotherm - regardless
 432 of whether the temperature transitions smoothly from one side of the damage front to the
 433 other or whether, like the damage front, it has a sharp transition - then the velocity of
 434 the damage front can be used to estimate the relative strengths of diffusive versus total
 435 (advective plus diffusive) heat transfer. Assuming that the damage front is far from r_0 and
 436 differentiating equation (2.49) with respect to time gives

$$437 \quad \frac{dR}{dt} \approx \frac{1}{2} \sqrt{\frac{2k_1 \Delta p r_0}{\mu \Delta \phi R_m t}}. \quad (4.8)$$

438 The velocity of a purely diffusive temperature front is roughly

$$439 \quad \frac{d}{dt} \sqrt{\kappa t} = \frac{1}{2} \sqrt{\frac{\kappa}{t}}, \quad (4.9)$$

440 where κ is the thermal diffusivity. Dividing 4.8 by 4.9 yields the dimensionless number

$$441 \quad \chi \equiv \sqrt{\frac{2k_1 \Delta p r_0}{\mu \Delta \phi R_m \kappa}}. \quad (4.10)$$

442 Assuming that $10^{-2} \leq \Delta \phi \leq 10^{-1}$ and using the values in Table 2, we obtain the result
 443 that $16 \leq \chi \leq 36$. Hence, the model predicts that advection is very significant compared to
 444 diffusion for this system.

445 Finally we note that, although we have not included the effects of thermal expansion on
 446 the density in equation (2.40), the error comitted is small as long as the fractional change
 447 in density is small. This is because the second term on the left side of the steady state mass
 448 balance equation

$$449 \quad \nabla^2 p + \frac{\nabla \rho}{\rho} \cdot \nabla p = 0, \quad (4.11)$$

450 is small compared to the first if $\Delta \rho / \rho_0$ is small compared to unity. Even in the present
 451 case of thermally driven damage, the fractional change in density is only on the order of ten
 452 percent; therefore, the error committed in neglecting the density variation is acceptable for
 453 the purposes of this study.

454 5. CONCLUSION

455 Damage induced by fluid injection modifies subsurface permeabilities and porosities, caus-
 456 ing both to be functions of pore pressure. Even though this dependence on pressure renders
 457 the mass balance equation nonlinear, we have been able to obtain a global analytic solu-
 458 tion for the pore pressure in the case of a vertical propagating damage front front via an
 459 analogy with the classical Stefan problem, where a moving surface of discontinuous material
 460 properties splits the solution domain into two parts. A formula was derived stating that
 461 gravitational effects may be ignored for sufficiently small times. We have also derived ap-
 462 proximate expressions for the position of the damage front as a function of time, which are
 463 valid for the cases of planar and spherical propagation front geometries. These expressions
 464 show that a thermally-induced damage front propagates much faster than one induced by

over-pressure, for the same values assigned to the model parameters. Finally, using these expressions, we derived approximate formulae for the surface flow rates under constant pressure injection for the case of spherical damage front geometry. When compared to recorded flow rate data from a particular site near Desert Peak, NV, our model suggests one possible interpretation of the data is that subsurface failure began at about five days after commencement of fluid injection, transitioning from the pre-damage regime to one of spherical damage front geometry over the course of 16 days.

ACKNOWLEDGEMENTS

This work was supported in part by the Department of Energy's Fossil Energy Program through the National Energy Technology Laboratory, and by the US DOE Office of Geothermal Technologies under Work Authorization No. GT-100036-12_Revision 1, EERE agreement No. 25316. This support is greatly appreciated. Satish Karra thanks U.S. Department of Energy for the support through the geothermal project DE-EE0002766. The authors would also like to acknowledge insightful review and comments by David Dempsey that led to significant improvements.

APPENDIX A. JUSTIFICATION FOR NEGLECTING $\nabla\rho$

Substituting (2.2), (2.3), and (2.4) into (2.1) yields

$$\tilde{\beta} \frac{\partial p}{\partial t} - \frac{k}{\mu} \frac{\rho}{\rho_0} \nabla^2 p - \frac{2kg\rho\beta}{\mu} \nabla z \cdot \nabla p - \frac{\beta k}{\mu} (\nabla p)^2 = 0, \quad (\text{A-1})$$

with

$$\tilde{\beta} \equiv \phi\beta + \frac{\rho}{\rho_0}\alpha. \quad (\text{A-2})$$

Dividing (A-1) by the term proportional to $\nabla^2 p$ leads to the dimensionless equation

$$\frac{\rho_0}{\rho} \left(\frac{\tilde{\beta}\mu}{k\nabla^2 p} \frac{\partial p}{\partial t} \right) - 1 - 2\beta\rho_0 g \frac{\nabla z \cdot \nabla p}{\nabla^2 p} - \frac{\rho_0}{\rho} \beta \frac{(\nabla p)^2}{\nabla^2 p} = 0. \quad (\text{A-3})$$

487 Now consider a small vertical section of porous material of height Δz over which the pressure
 488 varies by amount Δp , and suppose the time variation of p over an interval of time Δt is equal
 489 to $\xi \Delta p$ for some constant ξ . Then the first term on the left hand side is in order of magnitude

$$490 \quad \frac{\xi \tilde{\beta} \mu \Delta z^2}{k \Delta t}, \quad (\text{A-4})$$

491 where we have assumed that $\rho_0/\rho \approx 1$ and that the order of $\nabla^2 p$ is $\Delta p/\Delta z^2$. Term (A-4) is
 492 not in general small compared to unity. The third term has order of magnitude

$$493 \quad 2\beta \rho_0 g \Delta z, \quad (\text{A-5})$$

494 and due to the smallness of β , only approaches unity for very large values of Δz . The fourth
 495 term varies as

$$496 \quad \beta \Delta p, \quad (\text{A-6})$$

497 and is small compared to unity except for very large values of Δp . Therefore, for the
 498 parameter regime of interest in this study, the dominant balance in equation (A-1) is between
 499 the first and second terms on the left hand side.

500 REFERENCES

- 501 [1] Aharonov, E., and Anders, H., 2006, Hot water: a solution to the Heart Mountain detachment problem?,
 502 *Geology*, **34**, 165-168.
- 503 [2] Barenblatt, G. I., 1996, *Scaling, self-similarity, and intermediate asymptotics*, Cambridge Univarsity
 504 Press, pp. 412.
- 505 [3] Carslaw, H. S., and Jaeger, J.C., 1959, *Conduction of heat in solids*, Oxford University Press, USA, pp.
 506 520.
- 507 [4] Chabora, E., Zemach, E., Spielman, P., Drakos, P., Hickman, S., Lutz, S., Boyle, K., Falconer, A.,
 508 Robertson-Tait, A., Davatzes, N.C., Rose, P., Majer, E., and Jarpe, S., 2012, Hydraulic stimulation of
 509 well 27-15, Desert Peak Geothermal Field, Nevada, USA, *Proceedings 37th Workshop on Geothermal*
 510 *Reservoir Engineering*, SGP-TR-194.
- 511 [5] Dusseault, M. B., 2011, Geomechanical challenges in petroleum reservoir exploitation, *Journal of Civil*
 512 *Engineering*, **15**, 669-678.

- 513 [6] Geertsma, J., and de Klerk, F., 1969, A rapid method of predicting width and extent of hydraulically
514 induced fractures, *Journal of Petroleum Technology*, **21**, 1571-1581.
- 515 [7] Gordeyev, Y.N., and Zazovsky, A.F., 1992, Self-similar solution for deep-penetrating hydraulic fracture
516 propagation, *Transport in Porous Media*, **7**, 283-304.
- 517 [8] Jaeger, J. C., Cook, N.G.W., and Zimmerman, R.W., 2007, *Fundamentals of rock mechanics*, Blackwell
518 Publishing, pp. 473.
- 519 [9] Kohl, T., Evansi, K., Hopkirk, R., and Rybach, L., 1995, Coupled hydraulic, thermal and mechanical
520 considerations for the simulation of hot dry rock reservoirs, *Geothermics*, **24**, 345-359.
- 521 [10] Lee, H. S., and Cho, T.F., 2002, Hydraulic characteristics of rough fractures in linear flow under normal
522 and shear load, *Rock Mechanics and Rock Engineering*, **35**, 299-318.
- 523 [11] Lewis, K. C., Zyvoloski, G. A., Travis, B., Wilson, C., and Rowland, J., 2012, Drainage subsi-
524 dence associated with Arctic permafrost degradation, *Journal of Geophysical Research*, **117**, doi:
525 10.1029/2011JF002284.
- 526 [12] Lockner, D. A., Tanaka, H., Ito, H., Ikeda, R., Omura, K., and Naka, H., 2009, Geometry of the
527 Nojima Fault at Nojima-Hirabayashi, Japan - I. A simple damage structure inferred from borehole core
528 permeability, *Pure and Applied Geophysics*, **166**, 1649-1667.
- 529 [13] Mitchell, T. M., and Faulkner, D. R., 2012, Towards quantifying the matrix permeability of fault damage
530 zones in low porosity rocks, *Earth and Planetary Science Letters*, **339-340**, 24-31.
- 531 [14] Rubinstein, L.I., 1971, *The Stefan problem*, American Mathematical Society, pp. 419.
- 532 [15] Rutqvist, J., and Stephansson, O., 2003, The role of hydromechanical coupling in fractured rock engi-
533 neering, *Hydrology Journal*, **11**, 7-40, doi: 10.1007/s10040-002-0241-5.
- 534 [16] Voight, B., and Elsworth, D., 1997, Failure of volcano slopes, *Geotechnique*, **47**, 1-31.
- 535 [17] Wijesinghe, A.M., 1986, Similarity solution for coupled deformation and fluid flow in discrete fractures,
536 *International Conference on Radioactive Waste Management, Winnipeg, Manitoba, Canada, 7 Sep 1986*,
537 CONF-860910-2.
- 538 [18] Yow, J.L., and Hunt, J.R., 2002, Coupled processes in rock mass performance with emphasis on nuclear
539 waste isolation, *International Journal of Rock Mechanics and Mining Sciences*, **30**, 143-150.

TABLE 1. Comparison of closed form and numerical values of λ

$k_1(\text{m}^2)$	$k_2(\text{m}^2)$	ϕ_1	ϕ_2	closed form λ ($\text{ms}^{-1/2}$)	numerical λ ($\text{ms}^{-1/2}$)	rel. error %
10^{-12}	10^{-14}	0.101	0.1	2.116	2.109	0.3
10^{-12}	10^{-14}	0.2	0.1	0.213	0.213	2×10^{-2}
10^{-13}	10^{-14}	0.1001	0.1	1.979	1.929	2.6
10^{-13}	10^{-14}	0.3	0.1	4.759×10^{-2}	4.763×10^{-2}	6.8×10^{-2}
10^{-14}	10^{-16}	0.15	0.1	3.012×10^{-2}	3.013×10^{-2}	3.2×10^{-2}
10^{-15}	10^{-16}	0.152	0.15	4.671×10^{-2}	4.691×10^{-2}	0.4
10^{-12}	10^{-13}	0.152	0.15	1.477	1.484	0.4

TABLE 2. Parameters used to match the analytic solution to field data

Parameter	Value	Parameter	Value
k_1 (m^2)	1.2×10^{-13}	p_H (MPa)	13.1
k_2 (m^2)	10^{-14}	p_L (MPa)	9
ρ (kg/m^3)	980	r_0 (m)	0.23
μ ($\text{Pa}\cdot\text{s}$)	0.25×10^{-3}	b (days^{-1})	1
t_{shf} (days)	5	Δt (days)	3
t_{max} (days)	40		

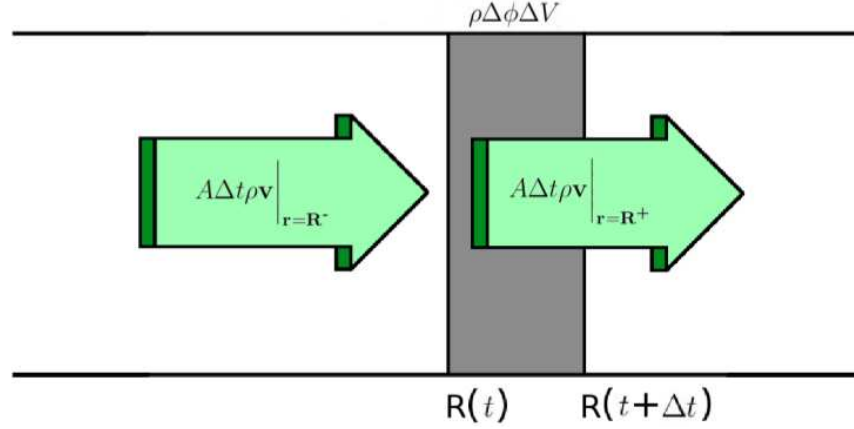


FIGURE 1. Representation of the mass balance condition (2.8). The mass of fluid flowing toward the damage front from the side of the damaged material equals the mass of fluid flowing away from the front into the undamaged material, plus the fluid taken up due to an increase in porosity as the front traverses a volume ΔV in time Δt .

540 COMPUTATIONAL EARTH SCIENCES GROUP, EARTH AND ENVIRONMENTAL SCIENCES DIVISION, LOS
 541 ALAMOS NATIONAL LABORATORY (LANL), LOS ALAMOS, NM 87545, UNITED STATES OF AMERICA
 542 *E-mail address:* `kaylal@lanl.gov` (K.C.Lewis);
 543 *E-mail address:* `satkarra@lanl.gov` (S. Karra);
 544 *E-mail address:* `kelkar@lanl.gov` (S. Kelkar)

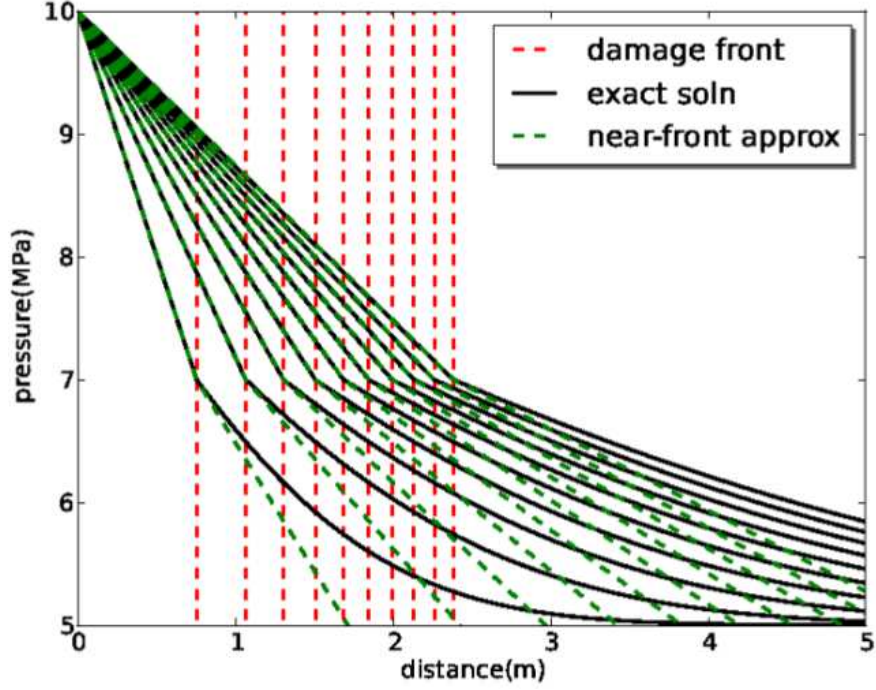


FIGURE 2. Representative pressure profiles calculated from (2.12) using $\mu = 10^{-4}$ Pa·s, $\Delta\phi = 0.01$, $\gamma = 10^{-10}$ Pa $^{-1}$, $k_1 = 10^{-13}$ m 2 , $k_2 = 10^{-14}$ m 2 , $p_H = 10$ MPa, $p_L = 5$ MPa, and $p_D = 7$ MPa. The profiles correspond to times of 1, 2, ..., 10 days. Red dashed lines indicate the distance of the damage front from the injection well. Green dashed lines show the approximate pressures used to estimate the derivative of the pressure directly adjacent to the damage front on each side. These lines lie directly on top of the exact solution in the zone of failed material.

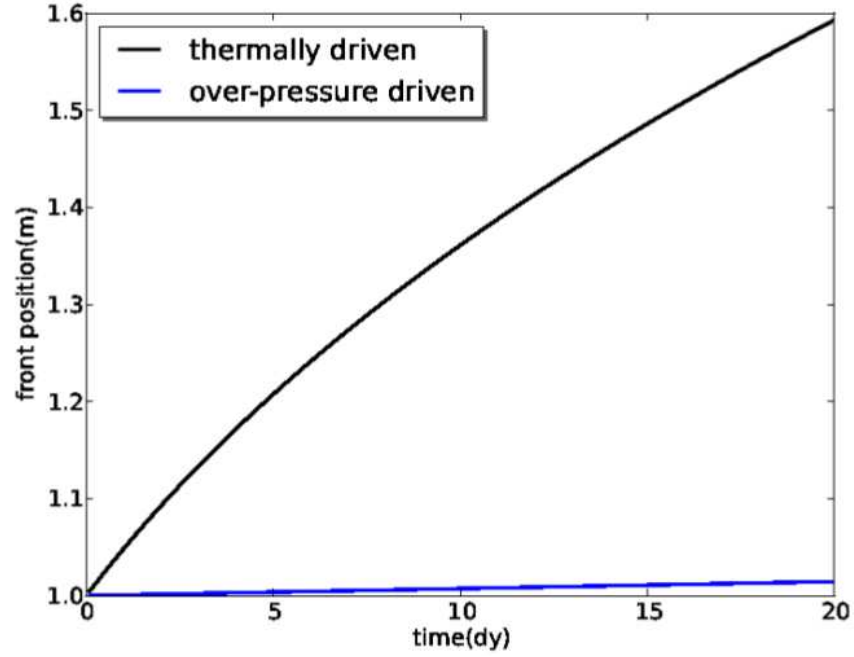


FIGURE 3. Comparison between the positions of spherical damage fronts due to over-pressure (blue) and due to thermal effects (black).

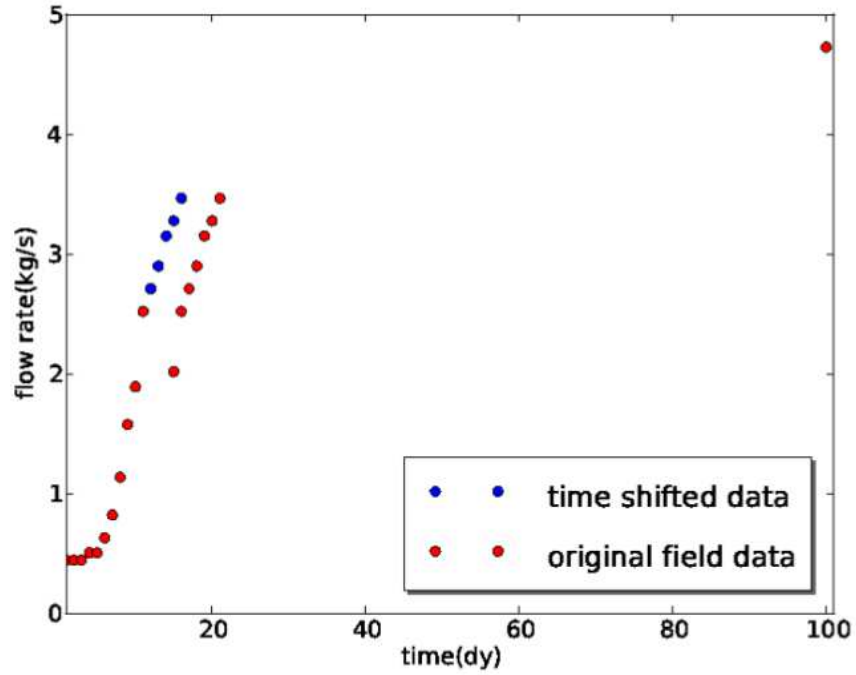


FIGURE 4. Flow rates obtained by Chabora et al. [4] during constant pressure injection of fluid at $T \approx 100^\circ\text{C}$ into rock at $T \approx 190^\circ\text{C}$ (red circles); data past eleven days shifted three days backward, and points overlapping with the earlier data removed (blue circles).

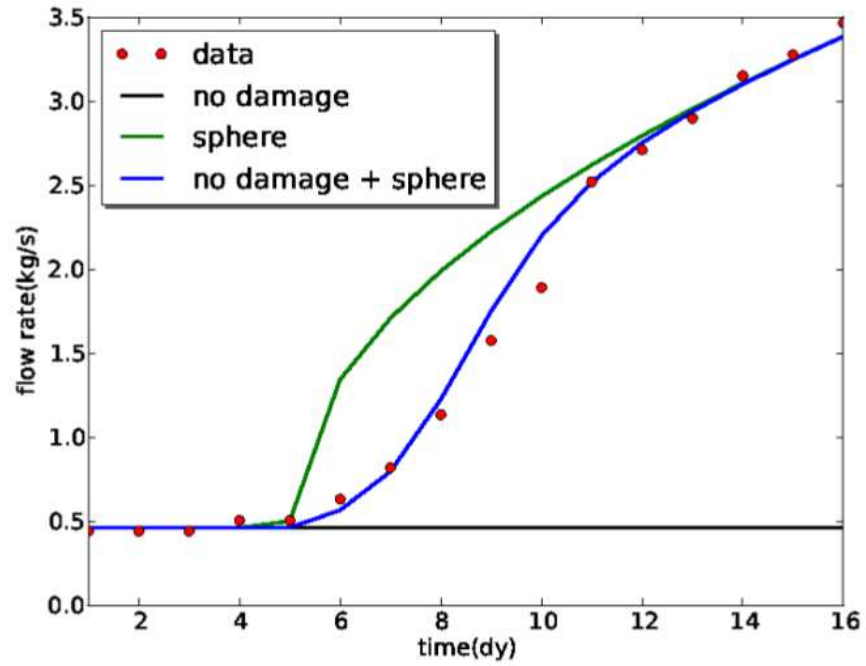


FIGURE 5. Comparison between the model solution (4.7, blue), flow rates expected in the case of no damage (black), flow rates expected from an expanding spherical damage front starting at five days (green), and the Desert Peak field data (red dots).